EDGE ARTICLE

Check for updates

Templating S100A9 amyloids on Aβ fibrillar surfaces revealed by charge detection mass spectrometry, microscopy, kinetic and microfluidic analyses†

Jonathan Pansieri, [ID] ‡[a] Igor A. Iashchishyn, [ID] ‡[a] Hussein Fakhouri,[b] Lucija Ostojić,[a] Mantas Malisauskas,[a] Greta Musteikyte, [ID] [c] Vytautas Smirnovas, [ID] [c] Matthias M. Schneider, [ID] [d] Tom Scheidt, [ID] [d] Catherine K. Xu,[d] Georg Meisl, [ID] [d] Tuomas P. J. Knowles,[de] Ehud Gazit,[af] Rodolphe Antoine [ID] [b] and Ludmilla A. Morozova-Roche [ID] *[a]

The mechanism of amyloid co-aggregation and its nucleation process are not fully understood in spite of extensive studies. Deciphering the interactions between proinflammatory S100A9 protein and Aβ$_{42}$ peptide in Alzheimer's disease is fundamental since inflammation plays a central role in the disease onset. Here we use innovative charge detection mass spectrometry (CDMS) together with biophysical techniques to provide mechanistic insight into the co-aggregation process and differentiate amyloid complexes at a single particle level. Combination of mass and charge distributions of amyloids together with reconstruction of the differences between them and detailed microscopy reveals that co-aggregation involves templating of S100A9 fibrils on the surface of Aβ$_{42}$ amyloids. Kinetic analysis further corroborates that the surfaces available for the Aβ$_{42}$ secondary nucleation are diminished due to the coating by S100A9 amyloids, while the binding of S100A9 to Aβ$_{42}$ fibrils is validated by a microfluidic assay. We demonstrate that synergy between CDMS, microscopy, kinetic and microfluidic analyses opens new directions in interdisciplinary research.

Introduction

In spite of the key clinical importance of amyloid formation, the mechanisms of co-aggregation of different amyloid species remain elusive. Amyloid formation is a widespread phenomenon routed in the generic property of polypeptide chains to self-assemble into cross-β-sheet containing superstructures[1,2] and manifested in numerous amyloid diseases[3,4] and functional amyloids.[5,6] Comorbidity of these diseases was reported to be

[a]*Department of Medical Biochemistry and Biophysics, Umeå University, SE-90187 Umeå, Sweden. E-mail: ludmilla.morozova-roche@umu.se*

[b]*Institut Lumière Matière, UMR 5306, Université Claude Bernard Lyon 1, CNRS, Univ Lyon, F-69100 Villeurbanne, France*

[c]*Institute of Biotechnology, Life Sciences Center, Vilnius University, Vilnius, Lithuania*

[d]*Centre for Misfolding Diseases, Department of Chemistry, University of Cambridge, Lensfield Road, Cambridge CB2 1EW, UK*

[e]*Cavendish Laboratory, Department of Physics, University of Cambridge, JJ Thompson Ave, CB3 0HE Cambridge, UK*

[f]*School of Molecular Cell Biology and Biotechnology, Tel Aviv University, Tel Aviv 69978, Israel*

† Electronic supplementary information (ESI) available: Experimental and computational details, 10 supplementary figures and 1 table. See DOI: 10.1039/c9sc05905a

‡ Authors with equal contribution.

linked to the co-aggregation of amyloidogenic proteins.[7,8] In Alzheimer's disease (AD), the amyloid-neuroinflammatory cascade is manifested in co-aggregation of Aβ with proinflammatory S100A9 protein, which leads to intracellular and extracellular amyloid assembly, amyloid plaque depositions and cellular toxicity.[9] S100A9 co-aggregates with Aβ also in traumatic brain injury, which is considered as a potential precursor state for AD.[10] The amyloid self-assembly of Aβ was well described by the involvement of secondary nucleation pathways promoted by Aβ amyloid surface.[11] In contrast, S100A9 undergoes nucleation-dependent autocatalytic amyloid growth.[12] There is a genuine unmet need to understand the architecture and mechanism of self-assembly leading to the formation of hetero-aggregates composed of various amyloid polypeptides. Since amyloids formed by individual polypeptides are highly polymorphic,[13–15] their co-aggregates add up to the complexity and heterogeneity of amyloid mixture. This complex problem has been addressed previously in a number of studies – the co-assembly of Aβ$_{40}$ and Aβ$_{42}$ was investigated by global kinetic analysis[16] and FTIR,[17] self-sorted supramolecular nanofibrils by *in situ* real-time imaging,[18] co-aggregates of wild-type α-synuclein with the familial mutant variant by dual-colour scanning for intensely fluorescent targets[19] and Aβ$_{42}$ peptide

Fig. 1 Templating S100A9 amyloids on $A\beta_{42}$ fibrillar surface revealed by AFM. (A–C) AFM images of (A) $A\beta_{42}$, (B) S100A9 and (C) $A\beta_{42}$–S100A9 amyloids. Scan sizes are 2×2 μm. Colour scale is represented on the right. 30 μM of each polypeptide were incubated individually or in mixture with each other for 24 h in PBS, pH 7.4 and 42 °C. Fibril length distributions of (D) $A\beta_{42}$ incubated separately, (E) $A\beta_{42}$ within $A\beta_{42}$–S100A9 complex, (F) S100A9 incubated separately and (G) S100A9 within $A\beta_{42}$–S100A9 complex. Probability mass function (PMF) defined as the probability of finding a fibril with a specific length is indicated along y-axes. Fibrillar lengths are indicated along x-axes. * The medians of fibril lengths with corresponding median deviations and sample sizes are shown within figures. The distributions are resampled to 10^4 (see Material and methods†).

consistent with the morphology of these short and coily fibrils observed by AFM and TEM (Fig. 1B and S5C, D†), and significantly lower in charges (55% – <0.36 ke) (Table S1†). It is worth noting that we were able to observe such low charged population of amyloid fibrils due to the improved signal to noise ratio of the home-built CDMS instrument (Materials and methods†). Indeed, the S100A9 fibrils display low charges compared to the charges on $A\beta_{42}$ fibrils observed here and in previous experiment as well as the charges on α-synuclein and tau fibrils reported previously.[25] The ranking of amyloid particles according to their CDMS z/m ratio for each amyloid sample (described in Materials and methods†) indicates that most of the individual fibrils of $A\beta_{42}$, S100A9 and $A\beta_{42}$–S100A9 are lower in charge than the corresponding monomers of $A\beta_{42}$ and S100A9; the monomer charges were calculated using their amino acid sequence at pH 7.4 (Fig. S6†). This is also consistent with previous data on the shielding of monomer charges within amyloid fibrils.[24] The population of particles with high masses in the S100A9 sample may reflect the clustering of few very flexible S100A9 fibrils into supercoils, as shown by TEM imaging (Fig. S5C and D†).

The frequency map of $A\beta_{42}$–S100A9 complexes deviates from those of individual $A\beta_{42}$ and S100A9 amyloids (Fig. 2G): 43% particles are <80 MDa and 20% are <0.36 ke (Table S1†). The distribution of data points is much broader in the $A\beta_{42}$–S100A9

frequency map and reflects partially the presence of free S100A9 fibrils in the sample as revealed by AFM (Fig. 1C, S1 and S2†). The slope of z to m corresponding to the population of $A\beta_{42}$–S100A9 complexes is intermediate between those for $A\beta_{42}$ and S100A9 fibril populations, respectively, which reflects the coating of $A\beta_{42}$ fibril surfaces by low charged S100A9 fibrils (Fig. 2E–G). The wide mass distribution may be related to the fact that S100A9 fibrils templated on $A\beta_{42}$ amyloid surfaces make them heavier and also by blocking $A\beta_{42}$ secondary nucleation, they promote $A\beta_{42}$ fibril elongation, as measured by AFM (Fig. 1D and E). At the same time S100A9 coating may also make the $A\beta_{42}$–S100A9 amyloids less prone to clumping. The presence of low m and high z complexes may reflect the population of $A\beta_{42}$ fibrils with surface bound S100A9 monomers, since they can bind to $A\beta_{42}$ fibrillar surface as we will discuss further.

In order to distinguish within the $A\beta_{42}$–S100A9 sample the sub-populations of joint hetero-molecular complexes and discriminate them from the sub-populations of individual fibrillar components, such as free $A\beta_{42}$ and S100A9 fibrils still present in this sample, we have advanced the CDMS methodology by building difference frequency distributions (described in Material and methods and shown in Fig. S4†). The difference frequency distribution maps were derived by comparing the following samples: pairwise $A\beta_{42}$–S100A9 and $A\beta_{42}$ (Fig. S7A and
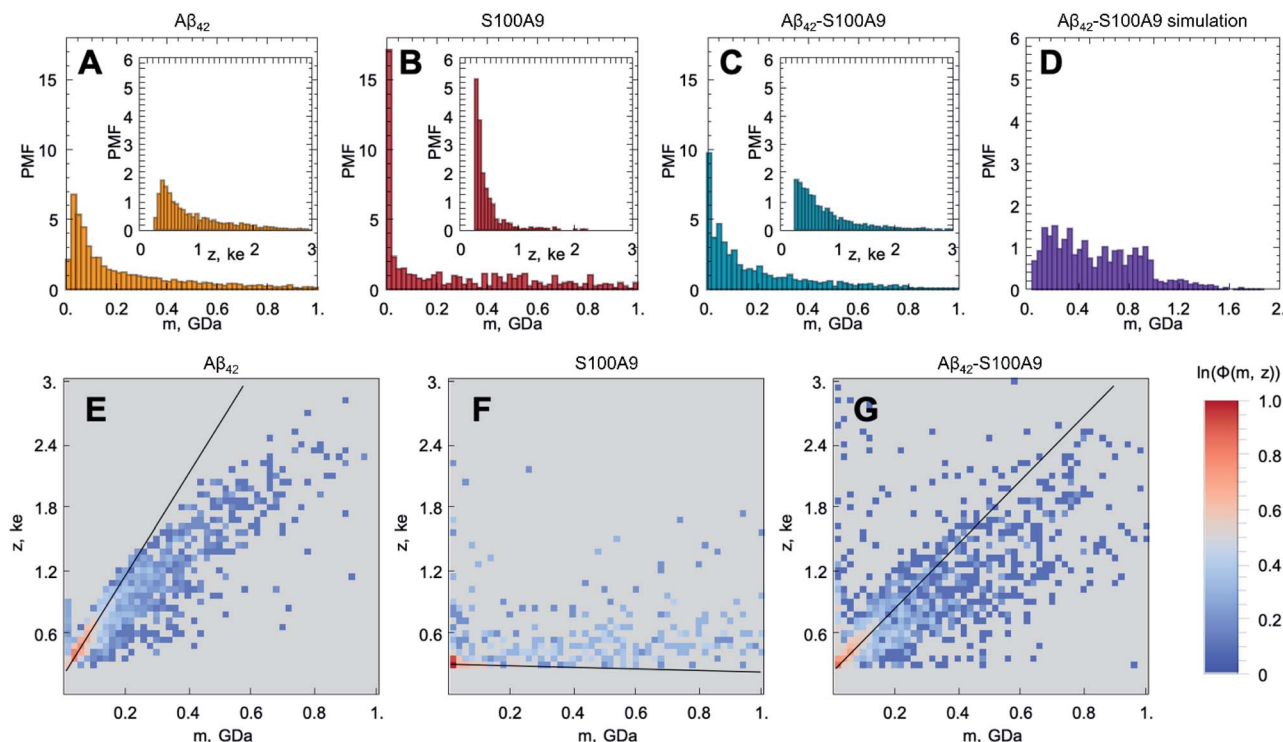
Fig. 2 Templating S100A9 amyloids on Aβ$_{42}$ fibrillar surface revealed by CDMS. Molecular mass (m) and charge (z, shown in insertions) distributions of (A) Aβ$_{42}$, (B) S100A9 and (C) Aβ$_{42}$–S100A9 amyloids. The CDMS distributions for Aβ$_{42}$ fibrils are shown in yellow, for S100A9 fibrils − in red and for Aβ$_{42}$–S100A9 amyloids − in blue. (D) Simulated molecular mass distribution for mixed Aβ$_{42}$ and S100A9 fibrils pre-incubated separately (shown in purple). The y-axes show probability mass function (PMF) defined as the probability of finding a fibril with the corresponding m or z, which are plotted along x-axes, respectively. (E–G) CDMS populations of amyloid particles are shown as frequency maps to demonstrate the probability of finding a particle with the corresponding m and z simultaneously: (E) for Aβ$_{42}$, (F) S100A9 and (G) Aβ$_{42}$–S100A9 amyloids. Colour scale is represented on the right.

D†); pairwise Aβ$_{42}$–S100A9 and S100A9 (Fig. S7B and E†) and Aβ$_{42}$–S100A9 *vs.* pair of Aβ$_{42}$ and S100A9 samples filtered out together (Fig. S7C and F†). This enables us to split the original CDMS data set into new sub-sets, demonstrating the enriched and depleted sub-populations of particles, respectively. Thus, by using this differential analysis we were able to filter out the component of interest, *i.e.* the sub-population of Aβ$_{42}$–S100A9 complexes, which is clearly distinct from both Aβ$_{42}$ and S100A9 amyloid sub-populations within the co-aggregated sample.

In addition, we have simulated the mass distributions of mixed Aβ$_{42}$ and S100A9 fibrils formed separately and then mixed together (described in Materials and methods†) and compared that with the observed CDMS mass distribution of Aβ$_{42}$–S100A9 co-aggregates as shown in Fig. 2C and D. The simulation demonstrates that the mass distributions of co-aggregated Aβ$_{42}$–S100A9 complexes and mixed pre-formed amyloids of Aβ$_{42}$ and S100A9 significantly deviate from each other. While the mixed fibrils are almost evenly distributed over broad range of molecular masses, the CDMS population of Aβ$_{42}$–S100A9 complexes displays exponential distribution. This further indicates that co-aggregation leads to a new type of joint complex formation.

In order to shed light on the co-aggregation mechanisms of Aβ$_{42}$–S100A9 complexes, we performed the kinetics analysis of S100A9 aggregation alone and Aβ$_{42}$ in the presence of

increasing S100A9 concentrations using a thioflavin T (ThT) fluorescence assay (Fig. 3A–C and S8A†). Aβ$_{42}$ fibrillation has been extensively studied previously and shown that it is governed not only by primary nucleation, but also by the secondary nucleation on the surface of already formed fibrils.[11,32] By contrast, S100A9 undergoes nucleation-dependent polymerization as we have demonstrated previously and does not involve secondary nucleation.[12,33] The kinetics of S100A9 fibrillation at different concentrations show that there is no noticeable lag-phase (Fig. 3A), indicating that the protein misfolding and primary nucleation is a rate-limiting step. The global fit results in the values of critical nuclei size, $n_c = 1.66$ and combined rate constant $k_n k_+ = 2.05 \times 10^4 \ \mu M^{-1.66} \ h^{-2}$.

The fibrillation curves of Aβ$_{42}$–S100A9 co-aggregation display typical sigmoidal shape (Fig. 3B) characteristic for fibrillation of Aβ$_{42}$.[11,32] Incubation of 2 to 100 μM S100A9 alone manifested in significantly lower ThT signal, if any, compared to the signal of ThT bound to Aβ$_{42}$ fibrils (Fig. S8A and B†). Therefore, in Aβ$_{42}$–S100A9 mixture the major ThT signal arises from dye molecules bound to Aβ$_{42}$ amyloids and those signals were used for fitting the fibrillation curves by the secondary nucleation dominated model as has been shown previously for Aβ$_{42}$.[11,32] The presence of S100A9 leads to increase of the lag-phase; the lowest 2 μM S100A9 concentration manifested in the most pronounced lag-phase increase to *ca.* 7 h, while 100 μM S100A9 results in *ca.* 4 h
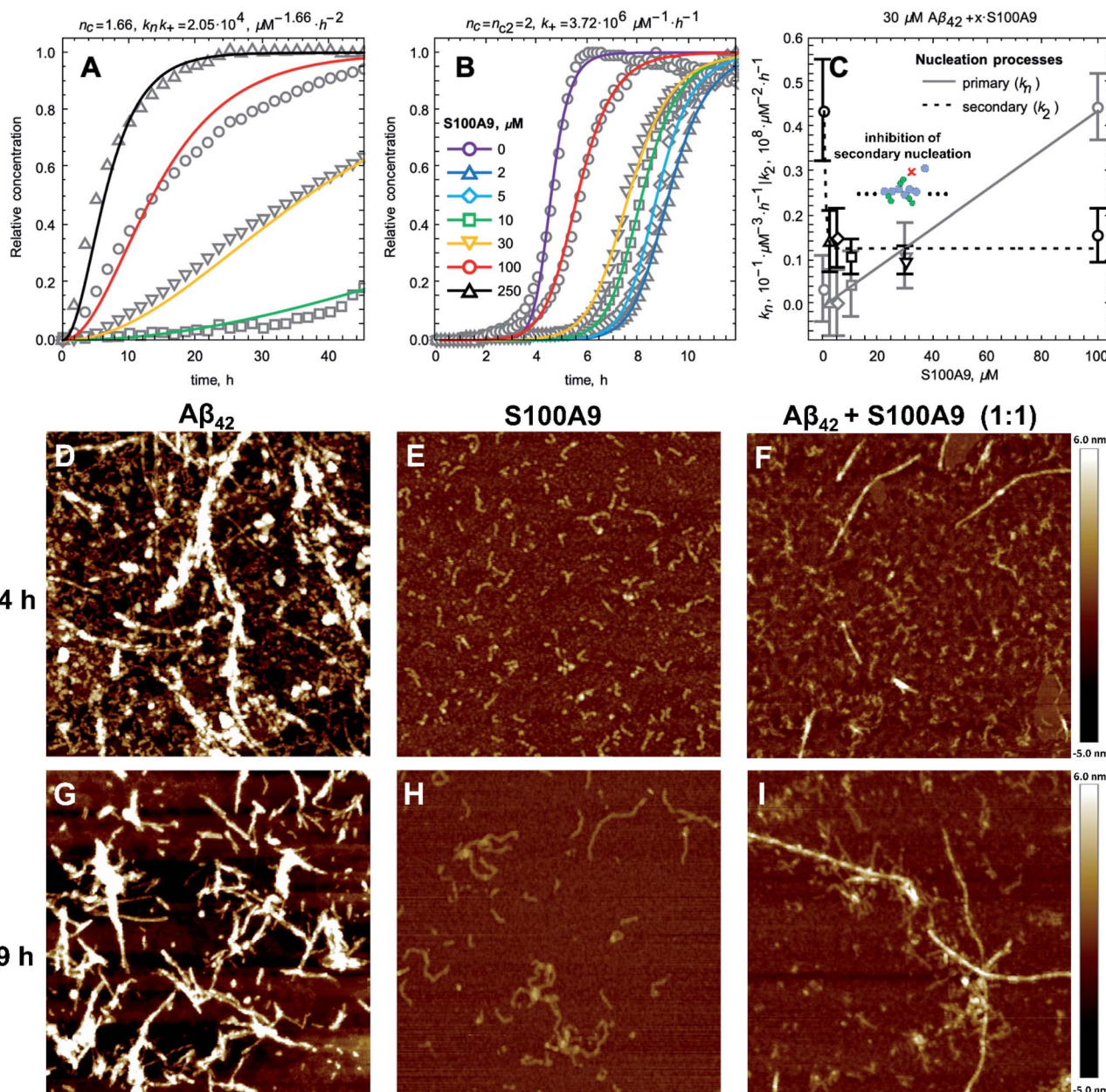
Fig. 3 S100A9 affects $A\beta_{42}$ primary and secondary nucleation pathways as revealed by the kinetic and AFM analyses. (A) Fibrillation kinetics of S100A9 monitored by ThT fluorescence and normalised to initial native S100A9 concentrations. Solid lines represent the global fitting by nucleation-dependent polymerisation model and experimental points are shown by grey symbols. (B) Normalised amyloid kinetics of $A\beta_{42}$ and S100A9 mixture monitored by ThT fluorescence and fitted by using a secondary nucleation dominated model. Solid lines represent the fitting curves and experimental points are shown by grey symbols. 30 μM $A\beta_{42}$, S100A9 concentrations are indicated in figure caption in corresponding colour coding (the same colour coding is used for (A) and (B)). Each solution contained 30 μM $A\beta_{42}$ and added S100A9 concentration, respectively. (C) Dependences of the primary nucleation, k_n (in solid grey), and secondary nucleation, k_2 (in dashed black), rate constants on S100A9 concentration as derived from the global fit presented in (B). AFM imaging of (D and G) $A\beta_{42}$, (E and H) S100A9 and (F and I) $A\beta_{42}$–S100A9 incubated for 4 h and 9 h, respectively, using 30 μM S100A9 and 30 μM $A\beta_{42}$, in PBS, pH 7.4 and 42 °C. Scan sizes are 2 × 2 μm. Colour scale is shown on the right.

lag-phase (Fig. 3B). In the presence of increasing S100A9 concentration the ThT plateau level of $A\beta_{42}$–S100A9 complexes decreases (Fig. S8A†). Most noticeable ThT signal decrease at highest S100A9 concentration in solution may reflect the coating effect of S100A9 species on the $A\beta_{42}$ amyloid surfaces. In the fitting of $A\beta_{42}$–S100A9 co-aggregation kinetics the

elongation rate, k_+, was set as a global fit parameter, *i.e.* shared for all fitted curves. The primary, k_n, and secondary, k_2, nucleation rates were set as fitting parameters, *i.e.* as variables for each of the fitted curves. Based on the reaction kinetic analysis we may conclude that the secondary nucleation rates for $A\beta_{42}$–S100A9 complexes are significantly reduced (Fig. 3C). This is in
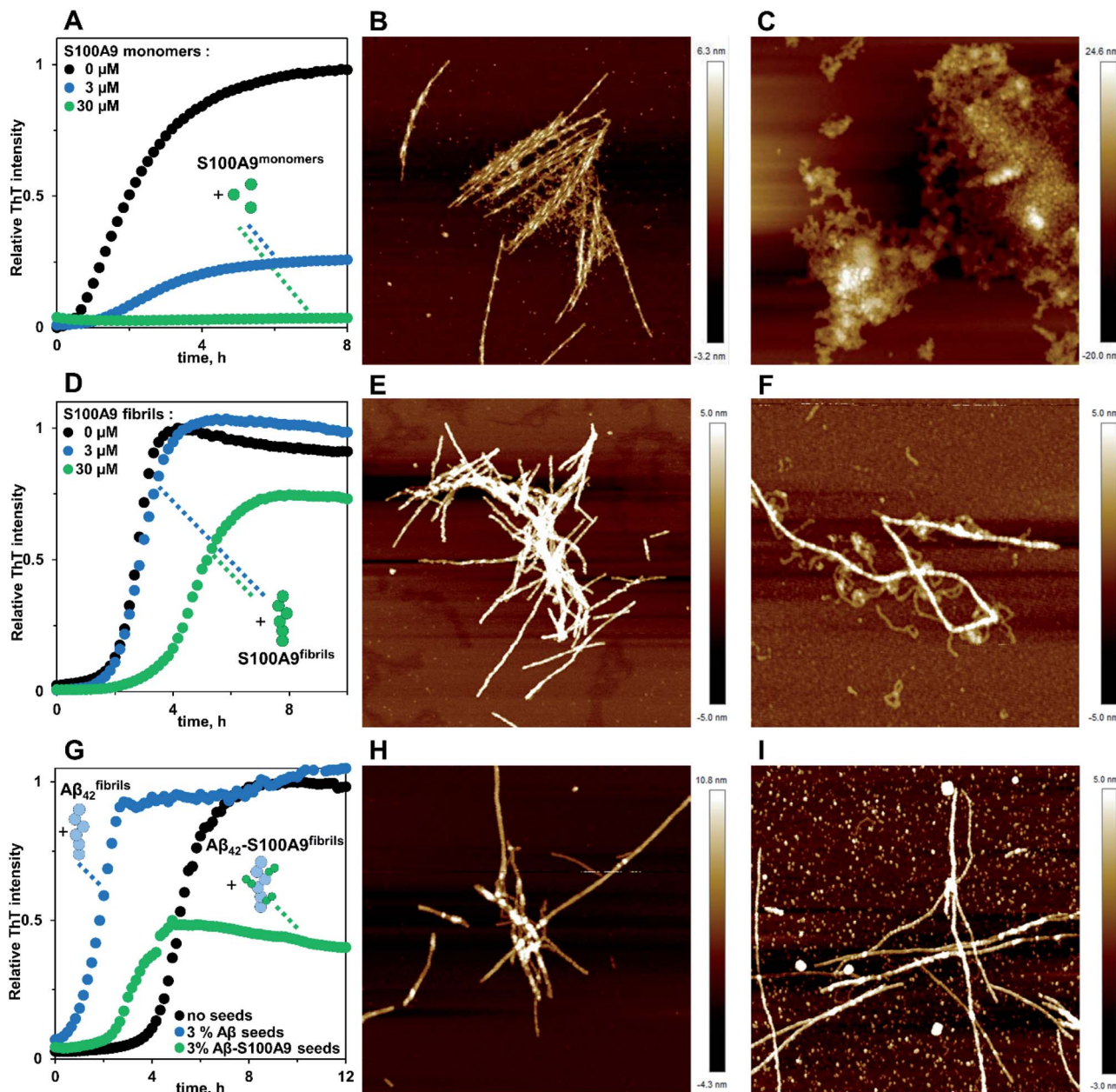
Fig. 4 Non-aggregating and fibrillar S100A9 produce different colour scale is shown on the right effects on Aβ$_{42}$ amyloid aggregation. (A) Fibrillation kinetics of the mixture of Aβ$_{42}$ and S100A9 monitored by ThT fluorescence, 10 mM HCl, pH 3, 42 °C. Concentrations of added non-aggregating S100A9 are indicated in figure caption in corresponding colour coding. AFM images of (B) Aβ$_{42}$ and (C) Aβ$_{42}$–S100A9 (1 : 1 molar ratio) aggregates observed after 24 h incubation. (D) Fibrillation kinetics of Aβ$_{42}$ in the absence and presence of S100A9 fibrillar seeds monitored by ThT fluorescence. Concentrations of added S100A9 fibrillar seeds are indicated in figure caption in corresponding colour coding. AFM images of (E) Aβ$_{42}$ and (F) Aβ$_{42}$–S100A9 (1 : 1 molar ratio) aggregates after 24 h incubation. (G) Fibrillation kinetics of Aβ$_{42}$ in the absence and presence of the fibrillar seeds of Aβ$_{42}$ and Aβ$_{42}$–S100A9. Added fibrillar seeds are indicated in figure caption in corresponding colour coding. AFM images of (H) Aβ$_{42}$ incubated with 3% Aβ$_{42}$ and (I) Aβ$_{42}$ with 3% Aβ$_{42}$–S100A9 seeds after 30 h incubation. 30 μM Aβ$_{42}$ was used in all experiments. Scan sizes are 2 × 2 μm.

agreement with the AFM observations of the increased length of Aβ$_{42}$ carrier fibrils templating S100A9 amyloid on their surfaces compared to Aβ$_{42}$ incubated alone (Fig. 1D, E and S2†). Interestingly, in the presence of 5 μM S100A9 in the mixture with Aβ$_{42}$, the length of Aβ$_{42}$ fibrils also increases, but to a smaller extend than in the presence of 30 μM S100A9; the median values of the corresponding length distributions are 0.68 μm vs. 0.75 μm, respectively, as presented in Fig. S2.† The fibril length can

be related to the rates of elongation and secondary nucleation[34] and, assuming that the change in fibril length observed here is due to a change in secondary rate alone, we obtain the following approximation for the change in fibril length, μ,

$$\frac{\mu_{A\beta_{42}}}{\mu_{mixed}} = \sqrt{\frac{k_{2,mixed}}{k_{2,A\beta_{42}}}} \qquad (1)$$
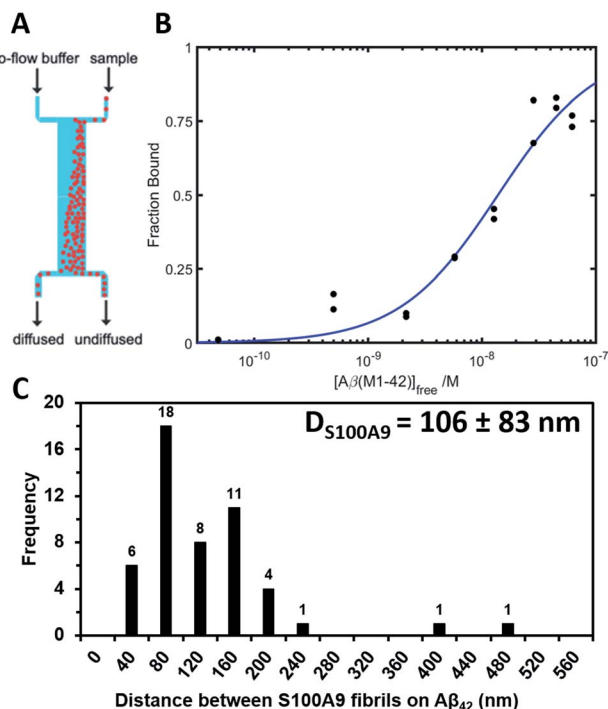
Fig. 5 Native S100A9 binding to $A\beta_{42}$ fibrils measured by microfluidic diffusional sizing. (A) Scheme of a microfluidic channel used to measure binding affinity between native S100A9 and $A\beta_{42}$ fibrils (Materials and methods†). (B) Binding curve for the interaction between S100A9 and $A\beta_{42}$ fibrils, from which dissociation constant and stoichiometric ratio were determined by Bayesian analysis. (C) Distribution of the distances between S100A9 fibrils templated on the surface of $A\beta_{42}$–S100A9 amyloids imaged by AFM. 30 μM of each polypeptide were co-incubated for 24 h in PBS, pH 7.4 and 42 °C.

Given the change in length observed by AFM (Fig. 1D and E), we thus expect a decrease of the rate constant of secondary nucleation, k_2, by approximately a factor of 3 in the presence of S100A9 compared to pure $A\beta_{42}$. Indeed, a decrease of k_2 by approximately this value is also obtained from analysis of the aggregation kinetics (Fig. 3C), showing that these two orthogonal measurements yield consistent results. Thus, the blocking of $A\beta_{42}$ fibrillar surfaces and its secondary nucleation by templating on them S100A9 fibrils leads to increase of their length.

By contrast, the distributions of lengths and heights of S100A9 fibrils remain the same (Fig. S2†) as whether they are fibrillated alone or in $A\beta_{42}$–S100A9 mixture, including both S100A9 filaments templated on $A\beta_{42}$ surfaces and free in solution. This indicates that as long as S100A9 fibrils were templated on $A\beta_{42}$ fibril surfaces, their size distributions are not affected by $A\beta_{42}$.

At the same time the higher rates of primary nucleation are consistent with the reduction of lag-phase of $A\beta_{42}$–S100A9 co-aggregation in the presence of S100A9 (Fig. 3B and C). The hydrophobic properties of S100A9 dimers and their larger effective cross-sections compared to these of $A\beta_{42}$ monomers may well serve also as nucleation sites for $A\beta_{42}$, especially if S100A9 itself undergoes amyloid self-assembly.[12,33] This implies that the effect of S100A9 on both primary and secondary

nucleation of $A\beta_{42}$ may depend on the degree of S100A9 polymerization.

AFM imaging was carried out in parallel to the amyloid kinetics to monitor amyloid development in time (Fig. 3D–I). After 4 h incubation $A\beta_{42}$ alone self-assembles into a large amount of protofibrils and mature fibrils (Fig. 3D), S100A9 forms very short filaments (Fig. 3E) and $A\beta_{42}$–S100A9 sample is characterized by both emerging $A\beta_{42}$-like fibrils, though in significantly smaller quantity compared to $A\beta_{42}$ incubated alone, and short protofilaments (Fig. 3F). After 9 h, $A\beta_{42}$ and S100A9 individually form their typical fibrils (Fig. 3G and H). By contrast, $A\beta_{42}$–S100A9 sample displays the mature thick fibrils, characteristic for $A\beta_{42}$, massively coated by distinct thin S100A9 filaments. They are present together with the short and thin filaments, characteristic for S100A9, in the surrounding solution (Fig. 3I), which is consistent with the corresponding images after 24 h incubation (Fig. 1C and S1†).

Further insights into the effect of non-aggregating S100A9 on $A\beta_{42}$ amyloid fibrillation was provided by incubating both polypeptides at pH 3.0, where $A\beta_{42}$ readily forms mature twisted fibrils (Fig. 4A and B), while S100A9 does not form amyloids at all (Fig. S9A and B†). In the presence of 3 μM non-aggregating S100A9, $A\beta_{42}$ amyloid formation is delayed, as reflected in an increased lag-phase and decreased both growth phase slope and ThT plateau level (Fig. 4A). $A\beta_{42}$ fibrillation is completely abolished in the presence of 30 μM S100A9, which is shown by both the absence of ThT signal and precipitation of unstructured aggregates observed by AFM imaging (Fig. 4C). The effects of the same concentrations of S100A9 fibrillar species on $A\beta_{42}$ fibrillation is less pronounced, *i.e.* 3 μM S100A9 fibrillar seeds do not significantly perturb the $A\beta_{42}$ fibrillation, while 30 μM seeds lead to some delay in amyloid formation and decrease in ThT fluorescence plateau (Fig. 4D). In the latter, $A\beta_{42}$ fibrils are coated with S100A9 amyloid filaments as observed in AFM image (Fig. 4F). This indicates that the surfaces available for $A\beta_{42}$ secondary nucleation are diminished by the presence of S100A9 amyloid coating, though S100A9 fibrillar species are less efficient in inhibiting $A\beta_{42}$ fibrillation than non-aggregated S100A9.

Co-incubation of $A\beta_{42}$ with 3% $A\beta_{42}$ fibrils produces pronounced seeding effect on $A\beta_{42}$ fibrillation, effectively abolishing the lag-phase and inducing mature fibril formation (Fig. 4G and H). By contrast, 3% $A\beta_{42}$–S100A9 co-aggregates are much less efficient in shortening the lag-phase, while causing nearly twice decrease of ThT plateau level and leading to the formation of fibrils and round-shaped aggregates (Fig. 4G and I). Since under the seeding conditions the $A\beta_{42}$ secondary nucleation pathways are dominant,[11] the $A\beta_{42}$–S100A9 seeds coated by S100A9 become less efficient than pure $A\beta_{42}$ fibrils. Noteworthy, in the control experiments, we demonstrate that S100A9 amyloid kinetics are not affected either by cross-seeding with $A\beta_{42}$ fibrils, even at 10% $A\beta_{42}$ seeds, or seeding with S100A9 fibrils (Fig. S9†).

The binding of native S100A9 to $A\beta_{42}$ fibrils was also examined by using a microfluidic diffusional sizing method as described in Materials and methods† and shown in Fig. 5A. The binding affinity of native S100A9 to $A\beta_{42}$ fibrils was determined

by measuring hydrodynamic radius, R_h, in the presence of increasing $A\beta_{42}$ fibril concentrations. The corresponding values of dissociation constant $K_d = 13.85$ (+9.11/−5.49) nM and stoichiometric ratio $a = 0.0035$ (+0.0010/−0.0007) nM were determined from the resulting binding curve (Fig. 5B). Such stoichiometric ratio corresponds to approximately one S100A9 binding site per *ca.* 300 $A\beta_{42}$ monomers in the $A\beta_{42}$ fibril. Based on the calculation of the number of monomers per unit of the $A\beta_{42}$ fibril length derived from the cryo-electron microscopy,[35] the distance between S100A9 binding sites on $A\beta_{42}$ fibril would be *ca.* 100 nm. AFM analysis indicates that the binding sites of S100A9 on $A\beta_{42}$ fibrils can be visualized with an average distance of *ca.* 100 nm between S100A9 filaments templated on $A\beta_{42}$ fibril in $A\beta_{42}$–S100A9 complexes (Fig. 5C and S10†). These numbers are broadly consistent with the stoichiometry determined by microfluidic diffusional sizing. Thus, by two independent methods we have demonstrated that the distance between the S100A9 binding and secondary nucleation sites on $A\beta_{42}$–S100A9 is about the same.

Conclusions

Inflammation is central to the onset of AD and many other neurodegenerative diseases, however the mechanistic insights into how inflammatory events are linked to the amyloid formation remain unclear. By using CDMS in combination with microscopy, kinetic analysis and microfluidic binding assay we have demonstrated that proinflammatory S100A9 protein, involved in AD and range of other neuroinflammatory and neurodegenerative diseases,[9,10,33] co-assembles with $A\beta$ fibrils, forming a new type of hetero-amyloid complexes. In these complexes the autocatalytic surfaces of $A\beta_{42}$ fibrils template S100A9 amyloids, where each component represents a homo-molecular domain in the hetero-molecular $A\beta_{42}$–S100A9 co-assembly. These change the dynamics of $A\beta$ amyloid aggregation and distribution of sizes of resulting co-assembled $A\beta_{42}$–S100A9 complexes. The formation of larger $A\beta_{42}$–S100A9 complexes may sequestrate smaller and more toxic species from the environment, which is consistent with our previous finding that co-aggregation of S100A9 with either $A\beta_{42}$ or $A\beta_{40}$ mitigate the overall amyloid cytotoxicity.[9] Thus, these findings contribute to understanding of amyloid co-aggregation processes both from a fundamental perspective and in revealing disease relevant processes.

Here we also exemplified analytical methods applied in synergy for the accurate analysis of such complex system as amyloid co-aggregation. We provide an analytical framework to utilize the capacity of CDMS, which can directly distinguish highly heterogeneous populations of amyloid co-aggregates in two dimensions, in combination with other biophysical techniques, assessing the bulk ensemble of molecular species, which together enable us to discriminate the amyloids originated from homo and hetero-molecular co-aggregation reactions. We have demonstrated the broad consistency in quantitative and qualitative measurements produced by those complementary techniques – CDMS and AFM (hetero-assemblies were observed by both methods); AFM and kinetic analysis (revealing the correlation between the fibrillar length and reduced secondary nucleation rates in the hetero-complexes) as well as microfluidic binding assay and AFM (consistency in stoichiometry of binding/templating of S100A9 on $A\beta_{42}$ fibrils).

The genuine understanding of the mechanisms underlying $A\beta_{42}$ and S100A9 driven amyloid-neuroinflammatory cascade in AD may also provide prospective target for therapeutic interventions and lead to the development of therapy for a cureless disease as the current approaches to target only one protein type did not mature.

Conflicts of interest

There are no conflicts to declare.

Acknowledgements

Notes and references

1 A. W. P. Fitzpatrick, G. T. Debelouchina, M. J. Bayro, D. K. Clare, M. A. Caporini, V. S. Bajaj, C. P. Jaroniec, L. Wang, V. Ladizhansky, S. A. Müller, C. E. MacPhee, C. A. Waudby, H. R. Mott, A. De Simone, T. P. J. Knowles, H. R. Saibil, M. Vendruscolo, E. V. Orlova, R. G. Griffin and C. M. Dobson, *Proc. Natl. Acad. Sci. U. S. A.*, 2013, **110**, 5468–5473.

2 M. Sunde, L. C. Serpell, M. Bartlam, P. E. Fraser, M. B. Pepys and C. C. F. Blake, *J. Mol. Biol.*, 1997, **273**, 729–739.

3 M. D. Benson, J. N. Buxbaum, D. S. Eisenberg, G. Merlini, M. J. M. Saraiva, Y. Sekijima, J. D. Sipe and P. Westermark, *Amyloid*, 2018, **25**, 215–219.

4 S. Shaham-Niv, L. Adler-Abramovich, L. Schnaider and E. Gazit, *Sci. Adv.*, 2015, **1**, e1500137.

5 D. Otzen and P. H. Nielsen, *Cell. Mol. Life Sci.*, 2008, **65**, 910–927.

6 D. M. Fowler, A. V. Koulov, C. Alory-Jost, M. S. Marks, W. E. Balch and J. W. Kelly, *PLoS Biol.*, 2005, **4**, e6.

7 I. Horvath and P. Wittung-Stafshede, *Proc. Natl. Acad. Sci. U. S. A.*, 2016, **113**, 12473–12477.

8 M. A. Burack, J. Hartlein, H. P. Flores, L. Taylor-Reinwald, J. S. Perlmutter and N. J. Cairns, *Neurology*, 2010, **74**, 77–84.

9 C. Wang, A. G. Klechikov, A. L. Gharibyan, S. K. T. S. Wärmländer, J. Jarvet, L. Zhao, X. Jia, S. K. Shankar, A. Olofsson, T. Brännström, Y. Mu, A. Gräslund and L. A. Morozova-Roche, *Acta Neuropathol.*, 2014, **127**, 507–522.

10 C. Wang, I. A. Iashchishyn, J. Pansieri, S. Nyström, O. Klementieva, J. Kara, I. Horvath, R. Moskalenko, R. Rofougaran, G. Gouras, G. G. Kovacs, S. K. Shankar and L. A. Morozova-Roche, *Sci. Rep.*, 2018, **8**, 1–16.

11 S. I. A. Cohen, S. Linse, L. M. Luheshi, E. Hellstrand, D. A. White, L. Rajah, D. E. Otzen, M. Vendruscolo, C. M. Dobson and T. P. J. Knowles, *Proc. Natl. Acad. Sci. U. S. A.*, 2013, **110**, 9758–9763.

12 I. A. Iashchishyn, D. Sulskis, M. Nguyen Ngoc, V. Smirnovas and L. A. Morozova-Roche, *ACS Chem. Neurosci.*, 2017, **8**, 2152–2158.

13 J.-P. Colletier, A. Laganowsky, M. Landau, M. Zhao, A. B. Soriaga, L. Goldschmidt, D. Flot, D. Cascio, M. R. Sawaya and D. Eisenberg, *Proc. Natl. Acad. Sci. U. S. A.*, 2011, **108**, 16938–16943.

14 R. Kodali and R. Wetzel, *Curr. Opin. Struct. Biol.*, 2007, **17**, 48–57.

15 C. M. Dobson, *Trends Biochem. Sci.*, 1999, **24**, 329–332.

16 R. Cukalevski, X. Yang, G. Meisl, U. Weininger, K. Bernfur, B. Frohm, T. P. J. Knowles and S. Linse, *Chem. Sci.*, 2015, **6**, 4215–4233.

17 M. Baldassarre, C. M. Baronio, L. A. Morozova-Roche and A. Barth, *Chem. Sci.*, 2017, **8**, 8247–8254.

18 S. Onogi, H. Shigemitsu, T. Yoshii, T. Tanida, M. Ikeda, R. Kubota and I. Hamachi, *Nat. Chem.*, 2016, **8**, 743–752.

19 A. Giese, B. Bader, J. Bieschke, G. Schaffar, S. Odoy, P. J. Kahle, C. Haass and H. Kretzschmar, *Biochem. Biophys. Res. Commun.*, 2005, **333**, 1202–1210.

20 N. Rezaei-Ghaleh, E. Andreetto, L.-M. Yan, A. Kapurniotu and M. Zweckstetter, *PLoS One*, 2011, **6**, e20289.

21 D. Z. Keifer, E. E. Pierson and M. F. Jarrold, *Analyst*, 2017, **142**, 1654–1671.

22 R. Antoine, *Rapid Commun. Mass Spectrom.*, 2020, e8539.

23 J. A. Hogan and M. F. Jarrold, *J. Am. Soc. Mass Spectrom.*, 2018, **29**, 2086–2095.

24 T. Doussineau, C. Mathevon, L. Altamura, C. Vendrely, P. Dugourd, V. Forge and R. Antoine, *Angew. Chem., Int. Ed. Engl.*, 2016, **55**, 2340–2344.

25 J. Pansieri, M. A. Halim, C. Vendrely, M. Dumoulin, F. Legrand, M. Moulin Sallanon, S. Chierici, S. Denti, X. Dagany, P. Dugourd, C. Marquette, R. Antoine and V. Forge, *Chem. Sci.*, 2018, **9**, 2791–2796.

26 M. Törnquist, T. C. T. Michaels, K. Sanagavarapu, X. Yang, G. Meisl, S. I. A. Cohen, T. P. J. Knowles and S. Linse, *Chem. Commun.*, 2018, **54**, 8667–8684.

27 G. Meisl, L. Rajah, S. A. I. Cohen, M. Pfammatter, A. Šarić, E. Hellstrand, A. K. Buell, A. Aguzzi, S. Linse, M. Vendruscolo, C. M. Dobson and T. P. J. Knowles, *Chem. Sci.*, 2017, **8**, 7087–7097.

28 S. I. A. Cohen, P. Arosio, J. Presto, F. R. Kurudenkandy, H. Biverstål, L. Dolfe, C. Dunning, X. Yang, B. Frohm, M. Vendruscolo, J. Johansson, C. M. Dobson, A. Fisahn, T. P. J. Knowles and S. Linse, *Nat. Struct. Mol. Biol.*, 2015, **22**, 207–213.

29 T. Scheidt, U. Łapińska, J. R. Kumita, D. R. Whiten, D. Klenerman, M. R. Wilson, S. I. A. Cohen, S. Linse, M. Vendruscolo, C. M. Dobson, T. P. J. Knowles and P. Arosio, *Sci. Adv.*, 2019, **5**, eaau3112.

30 R. Gaspar, G. Meisl, A. K. Buell, L. Young, C. F. Kaminski, T. P. J. Knowles, E. Sparr and S. Linse, *Q. Rev. Biophys.*, 2017, **50**, e6.

31 J. S. Jeong, A. Ansaloni, R. Mezzenga, H. A. Lashuel and G. Dietler, *J. Mol. Biol.*, 2013, **425**, 1765–1781.

32 G. Meisl, J. B. Kirkegaard, P. Arosio, T. C. T. Michaels, M. Vendruscolo, C. M. Dobson, S. Linse and T. P. J. Knowles, *Nat. Protoc.*, 2016, **11**, 252–272.

33 J. Pansieri, L. Ostojić, I. A. Iashchishyn, M. Magzoub, C. Wallin, S. K. T. S. Wärmländer, A. Gräslund, M. Nguyen Ngoc, V. Smirnovas, Ž. Svedružić and L. A. Morozova-Roche, *ACS Chem. Biol.*, 2019, **14**, 1410–1417.

34 S. I. A. Cohen, M. Vendruscolo, C. M. Dobson and T. P. J. Knowles, *J. Chem. Phys.*, 2011, **135**, 065106.

35 L. Gremer, D. Schölzel, C. Schenk, E. Reinartz, J. Labahn, R. B. G. Ravelli, M. Tusche, C. Lopez-Iglesias, W. Hoyer, H. Heise, D. Willbold and G. F. Schröder, *Science*, 2017, **358**, 116–119.